Optical to mid-IR observations of Lyman-α galaxies at z$\approx$5 in the HUDF: a young and low mass population

N. Pirzkal[1,2],S. Malhotra[3],J. E. Rhoads[3],C. Xu[4]

ABSTRACT

High redshift galaxies selected on the basis of their strong Lyman-α emission tend to be young ages and small physical sizes. We show this by analyzing the spectral energy distribution (SED) of 9 Lyman-α emitting (LAE) galaxies at $4.0 < z < 5.7$ in the Hubble Ultra Deep Field (HUDF). Rest-frame UV to optical 700Å $< \lambda <$ 7500Å luminosities, or upper limits, are used to constrain old stellar populations. We derive best fit, as well as maximally massive and maximally old, properties of all 9 objects. We show that these faint and distant objects are all very young, being most likely only a few millions years old, and not massive, the mass in stars being $\approx 10^6 - 10^8$ $M_\odot$. Deep Spitzer Infrared Array Camera (IRAC) observations of these objects, even in cases where objects were not detected, were crucial in constraining the masses of these objects. The space density of these objects, $\approx 1.25 \times 10^{-4}$ Mpc^{-3} is comparable to previously reported space density of LAEs at moderate to high redshifts. These Lyman-α galaxies show modest star formation rates of ≈ 8 $M_\odot$ yr^{-1}, which is nevertheless strong enough to have allowed these galaxies to assemble their stellar mass in less than a few $\times 10^6$ years. These sources appear to have small physical sizes, usually smaller than 1 Kpc, and are also rather concentrated. They are likely to be some of the least massive and youngest high redshift galaxies observed to date.

Subject headings: galaxies: evolution, galaxies: high redshift, galaxies: formation, galaxies: structure, surveys, cosmology

[1]Space Telescope Science Institute, 3700 San Martin Drive, Baltimore, MD 21218, USA

[2]Affiliated with the Space Science Telescope Division of the European Space Agency, ESTEC, Noordwijk, The Netherlands

[3]School of Earth and Space Exploration, Arizona State University, Tempe, AZ

[4]Shanghai Institute of Technical Physics, 500 Yutian Road, Shanghai, P.R. China 200083

1. Introduction

The availability of the Infrared Array Camera (IRAC) of the Spitzer Space Telescope, has recently made it possible to measure the rest-frame optical light from high redshift galaxies up to redshifts ≈ 6 (e.g. Yan et al. 2006; Chary et al. 2005; Egami et al. 2005; Eyles et al. 2005; Schaerer & Pelló 2005; Dow-Hygelund et al. 2005; Stark et al. 2006). Indeed, in just the past few years, a large numbers of Lyman Break Galaxies (LBG) and Lyman-α emitting galaxies (LAE) have been studied and IRAC data have enabled mass and age estimates for these objects to be derived. Historically, LBGs and LAEs are two distinct classes of objects that have been observed over a very wide range of redshifts, thanks in large part to the fact that these objects are relatively straight forward to identify via the presence of either a significant break in their spectral light distribution (LBG), or the presence of a strong Lyman-α emission line (LAE). As the number of known $z > 5$ LBGs and LAEs increased in the past few years (Yan et al. 2006; Eyles et al. 2005; Dawson et al. 2004, and references therein), the mass estimates of these objects have remained somewhat uncertain. Nevertheless observations have shown that some high redshift LBGs tend to be already quite massive ($> 10^{10}$ $M_\odot$), and to be a few 10^8 years old. The relatively large masses of these objects at a time when the Universe was still quite young, has been taken to be an indication that these objects have had a star formation history (SFH) that allowed for most of their stellar mass to have formed early on. Mass estimates for LAEs, on the other hand, have been much more difficult to assess. Either the LAEs are very young, as indicated by the strong Lyman-α line emission or the faintness of the continuum, for some other reason (for example, extinction), makes it difficult to derive mass estimates using their SED, as it is done for LBGs. Gawiser et al. (2006), for example, required the use of a stack of 18 field LAEs to infer an average mass of $\approx 5 \times 10^8$ $M_\odot$. This low estimated mass, and the low luminosity of these objects in the rest-frame optical, is exactly what makes estimating their masses somewhat more difficult than in the case of LBGs. While the later are usually selected based on broad band observations and colors, and hence ensures that these objects have bright continuum luminosities, LAEs selected via the presence of Lyman-α emission can be significantly fainter in the observed bands. For the handful of LAEs for which detections in IRAC have been obtained, a large mass in older populations has been derived (Lai et al. 2007; Chary et al. 2005). There is however a *detection bias* here: the only published mass/age estimates so far are the ones for which IRAC detections exist, i.e. they would tend to have significant old stellar populations.

In this paper, we investigate the population of high redshift LAEs in the Hubble Ultra Deep Field (HUDF, Beckwith et al. 2007), a field that is relatively small (11 sq. arcmin) but that has the advantage of having been observed down to very faint magnitudes, and in a wide range of wavelengths. Our LAEs sample makes no *a apriori* assumptions as to the

specific redshift of these sources, or as to whether these objects have been detected in all of the available data. We therefore aimed at reaching down to potentially fainter objects, and over a wider range of redshift, than previously done. Section 2 describes the object selection and the available data. In Section 3, we summarize the broad band luminosities of these objects, while in Sections 4, 5, and 6 we discuss the morphology, the SED fitting process, and provide mass and age estimates of the HUDF LAEs, irrespectively of wether these objects were detected in the Spitzer IRAC bands or not.

2. Observations

The sources described in this paper were selected from the GRAPES survey (GRism ACS Program for Extragalactic Science, PI: Malhotra, see description in Pirzkal et al. 2004), a slitless grism spectroscopic survey using the Advanced Camera for Survey (ACS) on the Hubble Space Telescope (HST). The GRAPES project obtained low resolution spectra of 1421 objects in the Hubble Ultra Deep Field (HUDF, Beckwith et al. 2007) down to a continuum level of $z_{850} = 27$ mag. The GRAPES grism observations proved to be able to detect emission lines with fluxes as low as $\sim 5 \times 10^{-18}$ erg s^{-1} cm^{-2} in objects as faint as $z_{850} = 29$ mag in the continuum. A complete list of GRAPES emission line objects was published by Xu et al. (2007) and contains 115 objects with redshifts $0.1 < z < 5.7$. GRAPES identified a total of 9 LAEs at $z > 4.0$ (Listed in Table 1). We show individual spectra of these 9 sources in Figure 1. In most cases, the spectra shown are a narrow extraction of the GRAPES program data. In two cases, where the galaxy is comparatively large, we show a wider extraction (5225 and 6139). Finally, in another two cases (631 and 9040), the GRAPES data have relatively few uncontaminated roll angles and we therefore plot instead spectra from the subsequent PEARS program (Probing Evolution And Reionization Spectroscopically, PI: Malhotra), which reobserved the HUDF in four new roll angles. The emission lines in the largest objects (6139, 9040, and especially 5225) are not shown to best advantage in these 1D extractions because the spatial extent of the object gives a wide line spread function in the slitless data, which tends to blur the line. Detailed 2D images of the observations of object 5225 are available in Rhoads et al. (2005). The GRAPES emission line object selection was performed automatically using an emission line search code and methodology described in details in Xu et al. (2007). Some of the objects shown in Table 1 have rather faint emission lines. All lines were nevertheless significant at the level of $3.1\sqrt{N/3}$ sigma, where N is the number of GRAPES position angles in which the line was detected, and where $N \geq 2$ was required for inclusion in Xu et al. (2007). For an emission line object to be classified as a Lyman-α galaxy, it had to also have (a) no other emission lines in the G800L grism wave-

length coverage[5], and (b) broad band photometry in the Hubble Ultra Deep Field images consistent with a Lyman break at the redshift corresponding to the Lyman-α line identification. Given less accurate photometry, a Lyman-α line plus Lyman break may be difficult to distinguish from an [OII] 3727Å line plus 4000Å break (Stern et al. 2000). Fortunately, even the faintest object in our sample is detected with s/n> 5 in two filters, and the rest are detected with s/n> 15 in two or more filters. This deep photometry shows that every object has a break where the flux is attenuated by a factor of at least 15 (See Table 3). The strengths of these breaks are several times greater than would be expected from the D(4000) break, and are much more consistent with the decrement expected from IGM absorption for objects at $z \approx 5$ (Madau 1995). Also, although it was not part of the GRAPES LAE selection process, these objects typically have very blue observed $z-J$ colors (corresponding to ~ 1400Å-1800Å restframe near UV colors), based on the NICMOS HUDF observations (Thompson et al. 2005). This makes it highly unlikely that any large amount of extinction is present in these objects, and so further supports the interpretation of their colors as a Lyman break at high redshift. Further spectroscopy could certainly help secure the redshifts and Lyman-α line identification for these objects. For example, higher resolution ($R \gtrsim 1000$) could help by verifying that the lines show the asymmetry characteristic of Lyman-α (e.g. Rhoads et al. 2003; Dawson et al. 2004). Similarly, bluer optical coverage could confirm the absence of other lines, and infrared coverage could confirm the presence of [OII] 3727Å at the same redshift as Lyman-α . However, all present evidence points to these objects being Lyman-α sources at $z \approx 5.5$.

The HUDF, which lays within the Great Observatories Origins Deep Survey field (GOODS, Giavalisco et al. 2004), has the advantage of having been observed in a wide range of wavelengths. In this paper, we take advantage of the availability of HST/NICMOS, VLT/ISAAC, and Spitzer IRAC observations of this field, as well as the list of 9 spectroscopically identified GRAPES LAEs. At the redshifts considered in this paper ($4.0 < z < 5.7$), combining these observations together allows us to examine these objects at the rest-frame wavelengths of approximately 700Å $< \lambda <$ 7500Å, and down to unprecedented depths. The ACS observations, using the B_{435}, V_{606}, i_{775}, and z_{850} bands each reach down to approximately 29 mag, with a final mosaic image resolution of 0.030" per pixel (Beckwith et al. 2007). NICMOS was used to observe a large sub-set of the HUDF in the near infrared (Thompson et al. 2005) using both the J and H bands. While the resolution of the NICMOS observations ($\approx 0.2''$ per pixel) is lower than that of the ACS observations, it is nevertheless high enough to clearly separate LAEs from their neighbors. We additionally used the VLT/ISAAC Ks band observations of the HUDF but the depth of these data is relatively shallow (25.1 mag)

[5]The case of Lyman-α plus CIV 1549Å emission did not occur in the GRAPES data set.

and with a resolution limited by atmospheric seeing (≈ 0.5"). Lastly, the HDUF was also observed in the infrared using IRAC as part of the GOODS Legacy Program (M. Dickinson et al. 2007 in preparation). While the latter observations have the relatively low resolution of 1.2" per pixel, they offer a unique opportunity to probe the rest-frame optical properties of $z \approx 5$ LAEs. The IRAC data reach down to a depth of nearly 26 mag in both the IRAC channel 1 (3.6μm) and channel 2 (4.5μm).

3. Photometry of Lyman-α emitters

The luminosity of each source was measured separately in each available band. Stamp images of the GRAPES LAEs are shown in Figure 2. Flux estimates were obtained using simple aperture photometry so that we could set meaningful upper limits to the flux of undetected sources, while the local noise level was estimated using small annulus surrounding each source. How we specifically dealt with non detections is explained in more details in Section 5. We used nominally sized apertures, each containing as much of the object flux as possible while minimizing the flux contributions from nearby objects, by additionally using an object catalog derived using the ACS $i_{775} + z_{850}$ data. The latter allowed us to verify that contamination from neighboring sources remained small.

Different aperture sizes were used in different bands. With the ACS data, we used an aperture size set to five times the size of the object as measured by Sextractor (Bertin & Arnouts 1996) (in this paper, apertures size refers to the diameter of the aperture), and no aperture correction was required. We verified that these measured fluxes agreed very well with Sextractor measurements and found that the two agreed to better than 1%. We used an aperture of 1.25" with the NICMOS data and applied aperture corrections of 1.06 and 1.09, in the J and H bands respectively (NICMOS Support 2007, personal communication). When measuring fluxes from the ground based ISSAC data, we used an aperture size that was twice as large as the size of the source, as measured in the ACS z image and after accounting for a seeing disk of 0.5". As discussed above, the IRAC data have both a lower resolution and suffer from a higher level of contamination from neighboring sources than the rest of our data. The IRAC photometric measurement process was therefore more involved than when using ACS, NICMOS, and ISAAC data. Since many of the GRAPES LAEs were only marginally resolved in the IRAC observations, and because contaminating flux from nearby objects would cause flux measurements to be systematically higher (leading to systematically higher masses, as we will discuss further later in this paper), we developed a technique to remove as much of the contaminating flux as possible. Our approach consisted in performing two dimensional general Sérsic profile fits of all neighboring sources (whose positions were derived using the ACS $i_{775} + z_{850}$ object catalog) using the program GALFIT (Peng et al. 2002).

Table 1. GRAPES LAEs and their morphological measurements. The half-light radius (R_{50}), Concentration (C), Asymmetry (A) and absolute magnitude ($M_{1500\mathring{A}}$) were estimated at a rest-frame wavelength of 1500Å. The redshifts and the line fluxes are from Xu et al. (2007). The line fluxes from Xu et al. (2007), shown using parenthesis, were corrected using aperture correction that we derived taking into account the size of each individual source.

UID	R.A.	Dec.	Redshift z	Flux 10^{-18} erg s^{-1} cm^{-2}	$M_{1500\mathring{A}}$	R_{50} (kpc)	C	A
631	3:32:40.09	-27:49:01.19	4.00	58. (20)	-20.21	0.67	2.74	0.097
712	3:32:42.81	-27:48:58.51	5.20	17. (6)	-21.31	0.52	2.53	0.11
4442	3:32:39.38	-27:47:39.17	5.76	24. (7)	-19.54	0.61	2.89	0.22
5183	3:32:34.51	-27:47:27.11	4.78	32. (11)	-19.82	0.54	2.84	< 0.1
5225	3:32:33.26	-27:47:24.76	5.42	22.[a]	-22.77	1.86	2.18	0.31
6139	3:32:37.95	-27:47:10.99	4.88	60. (22)	-22.14	1.35	3.19	0.41
9040	3:32:41.08	–27:46:42.45	4.90	36. (13)	-22.41	1.47	2.65	0.12
9340	3:32:40.67	-27:45:56.11	4.71	49. (15)	-20.52	0.66	2.69	0.89
9487	3:32:40.17	-27:46:00.55	4.10	55. (17)	-21.98	0.62	2.36	0.11

[a]From Rhoads et al. (2005)

The centermost 4" region surrounding each LAE source was masked and therefore not used during the fitting process. Each object was individually and interactively processed until the best possible fit was achieved, while avoiding to over subtract the flux contribution from the neighboring sources. Following this, the 2D models of the light profile of nearby sources were subtracted from the original IRAC images and aperture photometry was performed on the resultant images, just as we did with ACS, NICMOS, and ISAAC data. The reduced χ^2 of the GALFIT fitting of the nearby sources was usually near unity. In the few cases where nearby sources were not perfectly fitted using a Sérsic profile, we made sure that we did not end up over-subracting the amount of light contributed by these nearby objects. At the presumed redshifts of these objects, undersubtracting the contaminating light produced by nearby object ultimately results in an overestimate of the rest-frame optical GRAPES LAEs flux. This, in turn, can only lead to an inflation of the stellar mass estimates. We used a fixed aperture of 3" for all IRAC data, and applied aperture corrections of 1.78 and 1.77 to IRAC channel 1 and channel 2, respectively (Mobasher 2006, private communication). The IRAC aperture corrections were determined following extensive Monte Carlo simulations (Mobasher et al. 2005). Note that we did not use IRAC channels 3 and 4, as these proved a bit too noisy for our purpose. Table 3 shows the magnitude estimates of each source and in each available band, as well as the 3σ upper limit estimates for non-detection (shown with the $>$ symbol).

4. Morphology

We measured the size and morphology of each GRAPES LAE using both GALFIT (Peng et al. 2002) and the CAS parameters (Conselice et al. 2000). We computed the rest-frame size, concentration (C) and asymmetry (A) of each source separately in each of the available ACS bands. 1500Å rest-frame values of these parameters were then computed by interpolating these measurements.

The individual measurements are shown in Table 1. GRAPES LAEs are found to be sharply concentrated and asymmetric sources with average values of 2.67 ± 0.30 and 0.23 ± 0.30 for C and A, respectively. The half-light radius obtained using GALFIT are consistent with this, with an average size of 0.92 ± 0.50 kpc (or $0.17 \pm 0.07''$) while best fitting light profiles were sharp and concentrated in most cases. Three of the sources (5225, 6139, and 9040) are significantly larger than the rest of the GRAPES LAEs however, with an average half light radius of 1.56 ± 0.27 kpc, as shown in Figure 3. Moreover, two of these three objects (5225 and 6139) have larger measured asymmetry values than the rest of the sample. In general, objects with larger asymmetries are observed to be have large half light radius, raising the possibility that these objects could in fact be the result of smaller interacting components.

Table 2. GRAPES LAEs photometric measurements. Error estimates are shown in parenthesis. 3σ upper limits are indicated using the $>$ sign.

	ACS				NICMOS		ISAAC	IRAC	
UID	B_{435}	V_{606}	i_{775}	z_{850}	J_{1100}	H_{1600}	Ks_{2200}	$IRAC_{3600}$	$IRAC_{4000}$
631	29.59	26.87	26.41	26.47	26.49	26.76	>26.61	27.17	27.16
	(0.35)	(0.02)	(0.01)	(0.03)	(0.07)	(0.10)	(0.83)	(0.37)	(0.44)
712	31.48	29.66	27.25	27.12			26.74	28.05	>27.45
	(2.01)	(0.25)	(0.03)	(0.04)			(1.32)	(0.84)	(0.83)
4442	>32.96	31.64	29.35	28.36	29.48	30.63	>27.78	>28.53	>28.07
	(0.83)	(1.22)	(0.18)	(0.11)	(0.52)	(2.04)	(0.83)	(0.83)	(0.83)
5183	31.76	28.27	27.39	27.97	28.60	28.11	>27.33	>28.13	>27.85
	(2.04)	(0.06)	(0.03)	(0.09)	(0.28)	(0.20)	(0.83)	(0.83)	(0.83)
5225	28.88	28.29	25.97	25.93	26.05	26.68	26.54	26.51	25.86
	(0.41)	(0.17)	(0.02)	(0.04)	(0.07)	(0.16)	(1.62)	(0.28)	(0.26)
6139	>32.92	26.93	25.52	25.66	25.83	25.84	26.20	26.35	27.10
	(0.83)	(0.04)	(0.01)	(0.02)	(0.12)	(0.15)	(0.90)	(0.23)	(0.39)
9040	30.14	28.30	25.82	26.23	26.16	26.11	27.06	>28.45	>28.36
	(1.29)	(0.17)	(0.02)	(0.05)	(0.14)	(0.22)	(2.49)	(0.83)	(0.83)
9340	33.04	28.09	27.51	27.69			>27.40	>27.48	>27.16
	(0.83)	(0.05)	(0.03)	(0.07)			(0.83)	(0.83)	(0.83)
9487	30.07	27.25	27.16	27.27			>27.24	27.47	>27.93
	(0.47)	(0.02)	(0.03)	(0.05)			(0.83)	(0.47)	(0.83)

The only exception is object 9340 which, while small, is also quite irregular in shape. The estimated rest-frame 1500Å sizes are consistent with the expected sizes of objects at these redshifts as shown in Figure 1 of Ferguson et al. (2004) and Figure 7 of Pirzkal et al. (2006). As expected if the size of these objects scale approximately as H^{-1}, the GRAPES LAEs are indeed smaller than what was observed at lower redshifts by Ferguson et al. (2004). On the other hand, we found the mean ellipticity and concentration of the GRAPES LAEs are both marginally lower than what was measured and shown in Figure 3 of Ferguson et al. (2004). The mean GRAPES LAEs 1500Å ellipticity and concentration are observed to be 0.31 ± 0.18 and 2.67 ± 0.30, respectively.

Morphologically speaking, we observed GRAPES LAEs to be small, concentrated sources with somewhat irregular shapes, reminding us of local dwarf galaxies. The small sizes of the GRAPES LAEs is also similar to the sizes reported for $z \approx 6$ LBG by Dow-Hygelund et al. (2006). Several sources (5225, 6139, 9040, 9487) show a resolved clumpy/complex structure (44% of all sources) while 6 objects have an effective radius $R_{50} < 1.3$Kpc (67% of all sources). For comparison purposes with sources at a lower redshift, Venemans et al. (2005) found that, based on 40 $z \approx 3$ sources, 19% of their sample was observed to have clumpy structures, and 25% of their sources had an effective radius $R_{50} < 1.3$Kpc. Even considering the relatively low number involved, GRAPES LAEs appear to be systematically smaller, and maybe more irregularly shaped than LAEs at the lower redshift of $z = 3.1$.

5. Population Synthesis

The magnitudes shown in Table 3 provide us with unprecedented measurements of the rest-frame UV to optical light distribution of these faint high redshifts objects. A first glance, Table 3 shows these objects to be brighter in the i_{775}, z_{850}, J_{1100}, and H_{1600} bands (corresponding to the rest-frame of 1200Å $< \lambda <$ 2700Å) than in the IRAC bands (optical rest-frame wavelength of 6000Å $< \lambda <$ 7500Å) and than in the B_{435} and V_{606} bands (rest-frame UV of 700Å $< \lambda <$ 1100Å). The lack of strong emission in the B_{435} and V_{606} bands is due to HI absorption from the intergalactic medium (IGM) of these objects blue-ward of the Lyman-α limit.

It is worth emphasizing again that all LAEs were selected spectroscopically and that these sources were not selected using broad band colors. They nevertheless all exhibit very blue intrinsic colors, as shown in Figure 4, and appear to be significantly bluer than the LAE samples previously observed by Lai et al. (2007) and Eyles et al. (2005). One is immediately drawn to the possibility that these objects might well contain a population of active, young stars, which is of course consistent with the detection of Lyman-α emission in their GRAPES

spectra. There are no known X-ray emission within 5" of any of the sources presented here in the Chandra 1Ms observations of the field (Giacconi et al. 2002); which excludes the blue nature of these objects as being caused by an active galactic nucleus (AGN); confirming earlier conclusions of Malhotra et al. 2003, Wang et al. 2004, Gawiser et al. 2005.

A more quantitative determination of the age of these objects, or at least of the age of the stellar population of these objects, as well as an estimate of their stellar mass can be obtained by comparing the spectral energy distribution (SED) of these sources to stellar population synthesis models with known star formation history, masses, metallicities, and extinction values.

We compared the GRAPES LAEs SEDs to models from Bruzual & Charlot (2003, BC03), using the Padova evolutionary tracks, and using a Salpeter (1955) initial mass function (IMF). The choice of a Salpeter IMF allows us to directly compare GRAPES LAE mass estimates to ones previously published in the literature. It also allows us to view our results as upper limits to the stellar mass of the GRAPES LAEs: Because the Salpeter IMF continues as an unbroken power law to low stellar masses, it can overestimate the stellar masses of objects by a factor of two or more if there is a turnover at masses $\sim 1M_{\odot}$ (e.g. Baldry & Glazebrook 2003; Bell et al. 2003; Lai et al. 2007). The initial goal of this effort, and since many of the magnitudes listed in Table 3 are either upper limits or have large associated errors, was to determine whether some reasonable constraints could be set on some of the physical properties of these objects. i.e. we might not be in a position to unambiguously determine the exact nature of these objects, but we might be able to determine what they are likely *not* to be.

We used three different set of BC03 models, each using a different SFH: 1) A single instantaneous star formation burst (SSP); 2) A single, but exponentially decaying burst, with an e-folding time of τ (EXP); 3) Two separate instantaneous star formation bursts separated by an arbitrary amount of time, tburst, and with each burst contributing an arbitrary fraction of the final stellar mass of the galaxy (2BP). When using either of these three SFHs, the only free parameter that was allowed to vary during the fitting process was the total stellar mass of the model. The redshift, metallicity, age, and extinction were not treated as free parameters but as input assumption of the models.

Using each of these three SFH scenarios, we generated an extensive set of simulated spectra. Model spectra were computed at 27 discrete ages, ranging from as low as 5 Myr and up to the age of the Universe at the redshift of interest ($\approx$ 1.2Gyr, we adopt a ΛCDM cosmology throughout this paper with $\Omega_M = 0.3$, $\Omega_\Lambda = 0.7$, and $H_0 = 70$). The redshifts were fixed to the spectroscopically determined redshifts listed in Table 1. For the SSP and EXP SFH scenarios, we generated model spectra using several metallicity values (Z=0.0001, 0.0004, 0.004, 0.008, 0.02 ($Z_{\odot}$), and 0.05), and extinction values ($0 < Av < 3$, using the Calzetti Law, Calzetti et al. 2000). The 2BP models assumed a more restricted range of metallicities,

using a low metallicity for the first burst (Z=0.0001) and a solar metallicity (Z=0.02) for the second burst, but allowed for the same range of extinction values as the SPP and EXP scenarios. Differential extinction was not included in the 2BP model. We recognize the fact that the two stellar populations could in principle be subjected to different amounts of dust extinction. However, GRAPES LAEs are observed to be intrinsically very blue objects and hence to be objects that are dominated by a combination of young stars and low extinction. The data are not sufficient to allow us to study in details whether these two stellar populations do in fact suffer from slightly different amount of dust extinction. IGM absorption (Madau 1995) was added to all of the model spectra. A total of $\approx 80,000$ separate model spectra were generated at each of the 9 redshifts shown in Table 1

Considering each GRAPES LAE separately, we began the fitting process by minimizing the error-weighted χ^2 per degree of freedom (χ^2_ν) between observations and a particular model spectrum. During this step, a model spectrum was only allowed to be scaled up or down by an arbitrary amount, thereby determining the mass of the galaxy assuming that the model spectrum was a good fit to the observations. We only used bands where an object was detected, and we additionally excluded i_{775} band observations, that we knew to be contaminated by potentially a large, but uncertain, amount of Lyman-α emission. We did not attempt to simply correct the broad band i_{775} band measurements using the fluxes listed in Table 1 because of the large uncertainties associated with the aperture correction applied to the measured slitless spectroscopic fluxes. We also excluded the B_{435} and V_{606} bands that we knew to be strongly affected by IGM absorption.
This fitting process, while determining a mass estimate for each object, did not however take into account any of the upper limit estimates in cases of non detections. We incorporated this additional information in two distinct ways. First, we computed the Kendall rank correlation value for censored data sets (Isobe et al. 1986) between individual models (each scaled to best fit bands where the object was detected) and the observations. This method allowed to quantitatively determine how badly upper limit constraints might be violated by a particular model, but it had the drawback of not being able to take into account the errors in the flux measurements. It had the additional drawback of producing a goodness of fit estimator that was strongly quantized due to the limited number of available measurements. While models that strongly violated upper limit constraints could be identified, many of our models led to similar Kendall correlation values, making it difficult to select one model over another. We therefore also relied on another second that was based on a more generalized version of the error weighted χ^2_ν described above. This method took into account upper limit estimates and assigned a χ^2_ν penalty when a model predicted flux values that exceeded established upper limit values ($\chi^2_{\nu c}$). The value of this additive penalty is

$-\ln(\mathrm{I})$ where $\mathrm{I} = \mathrm{P}(< \sigma|\mu)$ is the probability that the actual flux is less than σ if the flux is assumed to be normally distributed with mean μ and width σ, where σ is the flux detection limit of the data and μ is the flux of the model in that bandpass. This method was used in Lai et al. (2007) where it is described in more details. We found a good agreement between the Kendall rank method and the $\chi^2_{\nu c}$ method, and both methods could indeed be used to reject models that over predicted fluxes in non detected bands. However, and because the $\chi^2_{\nu c}$ method allowed us to take flux measurements into account, which was crucial for some data points (such as the relatively low signal to noise ISAAC Ks observations), we eventually relied more on the $\chi^2_{\nu c}$ method. Models were thus rejected by first computing individual $\chi^2_{\nu c}$ values and then subsequently determine whether a given $\chi^2_{\nu c}$ value was an indication that a model was a statistically bad fit to the observations. The exact cut-off value of $\chi^2_{\nu c}$ used to reject a set of models was determined separately for each object since the number of bands used to compute $\chi^2_{\nu c}$ differed from one object to the next. We defined $P(\chi^2_{\nu c} > \chi^2_{\nu c_0})$ as the probability of obtaining a value of $\chi^2_{\nu c}$ as large as the observed $\chi^2_{\nu c_0}$, if the observations really did follow the assumed distribution (See Taylor 1997). We then assumed that observations and models differed *significantly* when $Prob_d(\chi^2_{\nu c} > \chi^2_{\nu c_0})$ was less than 5% (2σ level) and rejected the corresponding model on the basis that it was a poor fit to the observations. Models that could fit the observations could often be identified, using either of the three SFH scenarios that we considered. Some notable exception are objects 4442 and 5183 that we found to be somewhat poorly fitted by all of the models that we generated. Cut-off values of $P(\chi^2_{\nu c} > \chi^2_{\nu c_0})$ were therefore loosened for these two objects, and hence the selected best fits for these objects have higher $\chi^2_{\nu c}$ values than the rest of the GRAPES LAEs.

It is important to stress that we found that properly accounting for the non detection of an object, particularly in the IRAC bands, was crucial when attempting to either include or exclude a particular set of models. The IRAC fluxes, especially the ones that we corrected for the effect of neighbor contamination, allowed us to determine an upper limit to the optical rest frame flux emitted by the source. We found that such an upper limit imposed a strict upper limit to the number of older stars that can be accounted for in that object. This in turn allowed us to exclude a large subset of our original models. In the following section, we examine the mass estimates of the GRAPES LAEs and further summarize the range of acceptable input BC03 parameters.

6. Mass and Age

As expected with such a large number of input parameters, we found that a wide range of BC03 models provided an adequate fit to the observations. While a best fitting model could always be identified by simply selected the model with the lowest value of $\chi^2_{\nu c}$ (which we call the Best Fit model), we also determined the largest mass estimate and the oldest age estimate of each GRAPES LAE by simply examining the subset of BC03 models, and hence the corresponding parameters that went into creating these models, that were not rejected at the 2σ level. The model producing the best fit to observations was not always the most massive, nor the oldest model that properly fitted the observations. We defined the Maximum Mass models and the Maximum Age models as the models with the largest mass and ages, respectively that are good fits the observations (e.g. 2σ level or higher when possible, or highest possible confidence otherwise).

Table 3 summarizes our results using the SSP SFH scenario. This is a simple model that assumed that all the stars were created in a single burst event and then simply passively evolved. Examining the best fit models shown in Table 3, we found that all LAEs appeared to have very young stellar populations (few 10^6years) and low stellar masses, with only one object (6139) having a mass estimate that exceeded 10^8 $M_\odot$. Extinction values were consistently low while the metallicities were found to be sub-solar in the most cases. However, it should be noted that metallicity was not well constrained and that a wide range of metallicities were found to be acceptable. Naturally, a wider range of models were found to properly fit the observations and the masses and ages of the GRAPES LAEs could possibly be somewhat larger than those of the best fit models, as shown on the right end side of Table 3. Similarly, a range of age estimates were found to be acceptable. Yet, we found that acceptable ages remained below a few 10×10^6 year while masses remained below a few times $\approx 10^8$ $M_\odot$). Note that none of our BC03 models successfully fitted objects 4442, 5183, and 9040 ($P(\chi^2_{\nu c} > \chi^2_{\nu c_0}) < 5\%$), and that hence all of our BC03 models could formerly be rejected at the 2σ level. In these cases, Table 3 shows the model with the highest possible confidence level.

Tables 4 is similar to Table 3 but shows the results obtained using the EXP SFH scenario. In this scenario, star formation occurred in a burst that was not instantaneous but instead exponentially decayed as a function of time, with an e-folding time of τ. Unlike the previous SSP model, not all of the stars have the same ages in this scenario, and this scenario allowed for an increasingly larger proportion of stars to be older as the galaxy aged. The EXP models would therefore be expected to result in slightly larger age and mass estimates that the SSP scenario. As shown in Table 4, this is indeed marginally the case. The maximum

ages, shown in Table 4 are found to be in some cases up to a factor of ten time larger than those produced using the SSP scenario. The maximum masses however did not exceed a few $\times 10^8 M_\odot$, and were only slightly larger that the maximum masses derived using the SSP model and .

The mass and ages estimates derived using our third SFH scenario (2BP), are shown in Table 5. By design, the two-burst scenario was conceived to allow us to fit the SED of objects that are intrinsically very blue in their rest-frame UV light, yet appear to produce a significant amount of light in the rest-frame optical. The 2BP scenario allows for the presence of two distinct stellar populations, one young and blue and another older and therefore relatively redder. This scenario should therefore provide better fits to observations with both large ACS and IRAC fluxes. It should also be expected to yield higher mass estimates in cases of high upper flux limits in the IRAC bands. This scenario is similar to the Dickinson et al. (2003) maximally old population model. As shown in Table 5, the age estimates derived from the best fit to the data are in some cases significantly larger than the ones derived using either the SSP or EXP scenarios. This is of course achieved by allowing a significant fraction of the stellar population of the galaxy to be in the form of a maximally old ($>$ 1Gyr) population of stars. As previously observed, extinction values were low, and we found that lower extinction values were generally preferred using this SFR scenario. But we did find that a range of extinction values and burst mass ratios could fit the observations, leading to larger mass estimates, as long as at a few $\times 10^6$ $M_\odot$ of the galaxy mass was in the form of a young stellar population with an age of $\approx 5 - 35 \times 10^6$ year. The younger stellar population accounts for the significant UV flux in these object, while the much older (often up to the age of the Universe at the object redshift) account for an increase of the total mass of the galaxy by a factor of about two, when compared to the maximum mass SSP results. Figure 5 shows the best fit 2BP models for each GRAPES LAE (solid line), as well as the maximum mass select from models that were not rejected at the 2σ level (dashed line). Note that as we mentioned earlier three of the GRAPES LAE sources (4442, 5183, 9040) are not very well fitted by any of our chosen models. It is worth addressing again the possibility that one, or possibly more, of these three objects could be low redshift interlopers. However, and as pointed out in Section 2, every single one of these three objects has a very significant color break, consistently with what we would expect from IGM absorption at high redshifts, as well as very blue observed z_{850}-J_{1100} colors. We performed additional simulations of the expected B_{435}-z_{850} and z_{850}-J_{1100} colors of these objects if they were at much lower ($z \approx 0.25 - 0.5$) redshifts, assuming that the detected line was not Lyman-α but [OIII] 5007Å, and that the color break was the result of the D4000Å break. We concluded that the presence of a strong D4000Å break, together with a very blue rest-frame near-UV color, cannot be properly accounted by anything but a young stellar population at high redshift, independently of the

amount of extinction present, of the metallicity of the stellar population, and of the age of the stellar population. The latter led us to favor the interpretation that objects 4442, 5183 and 9040 are indeed very faint high redshift Lyman-α emitters. We recognize however that future high resolution spectroscopy will be required to unequivocally address this issue.

7. Discussion

Based on the detection of 9 Lyman-α sources in the HUDF, and using a $1/\mathrm{V_{max}}$ methodology, we derived a mean number density of $\approx 1.25 \pm 0.04 \times 10^{-4}$ Mpc^{-3}. Comparison with previous studies of high redshift Lyman-α sources is difficult since each study has slightly different limiting Lyman-α line fluxes and luminosities selection biases. This work in particular does not claim to be a complete sample of LAEs at these redshifts. Still, down to a limiting Lyman-α line luminosity of 2.0×10^{42} erg s^{-1}, Taniguchi et al. (2005) found that the density of $z \approx 6.6$ Lyman-α sources is 1.2×10^{-4} Mpc^{-3}. They furthermore estimated, based on observations from Ouchi et al. (2003), that the density of $z = 4.9$ Lyman-α sources is 2×10^{-4} Mpc^{-3}, down to the same line luminosity limit. At somewhat lower redshifts, Gawiser et al. (2006) recently estimated that the number density (again down the same limiting line luminosity limit) of $z = 3.1$ Lyman-α sources is $(3 \pm 1) \times 10^{-4}$ Mpc^{-3}. If we restrict our sample to the Taniguchi et al. (2005) limiting line luminosity, we still detected all 9 sources and the HUDF LAEs density remains $\approx 1.25 \pm 0.04 \times 10^{-4}$ Mpc^{-3}, which is consistent with previous works. Similarly, we can also compare our observations to the results from Rhoads & Malhotra (2001) at $z = 5.7$. The latter observations were carried out down to the brighter line luminosity limit of 5.3×10^{42} erg s^{-1}. In their work, Rhoads & Malhotra (2001) inferred a $z = 5.7$ Lyman-α density of $\approx 4 \times 10^{-5}$ Mpc^{-3}. Down to the authors brighter line luminosity limit, we detected 7 LAEs (631, 4442, 5183, 6139, 9040, 9340, 9487) and derive a Lyman-α density of $9.68 \pm 0.04 \times 10^{-5}$ Mpc^{-3}. Similarly, in this case, Taniguchi et al. (2005) computed a $z \approx 6.6$ Lyman-α object density of 2×10^{-5} Mpc^{-3} while the $z \approx 4.9$ object density from Ouchi et al. (2003) becomes 4×10^{-5} Mpc^{-3}. Our observations therefore confirm the relatively low value of the space density of Lyman-α sources objects at these high redshifts, as seen also by Malhotra & Rhoads (2004), confirms an apparent lack of, or at least slow, redshift evolution of the density of LAEs.

We found that, no matter which SFR scenario we considered, the GRAPES LAEs were unlikely to be very massive. Both the single instantaneous burst (SSP) and the exponentially decaying burst (EXP) scenarios resulted in similarly low mass estimates, the best EXP mod-

Table 3. Best single instantaneous burst SFH (SSP) fits to our observations. This table lists the age, mass, extinction, and metallicity that resulted in the lower values of $\chi^2_{\nu c}$. Objects that failed to be properly fitted at the 95% confidence level are indicated with a *.

UID	Age 10^6yr	Mass $10^8 M_\odot$	Av	Z $\%Z_\odot$	$P(\chi^2_{\nu c} > \chi^2_{\nu c_0})$	$\text{Age}_{\max}$ 10^6yr	$\text{Mass}_{\max}$ $10^8 M_\odot$
631	5.0	0.43	0.6	2.0	52.48	45.0	2.4
712	3.5	0.047	0.0	100.0	93.21	45.0	2.1
4442*	2.5	0.026	0.0	2.0	1.00	2.5	0.026
5183*	2.5	0.17	0.6	2.0	3.46	2.5	0.17
5225	4.5	0.21	0.0	0.5	56.30	9.0	0.45
6139	20.	3.2	0.4	0.5	78.91	30.0	5.0
9040*	2.5	0.15	0.0	0.5	0.05	2.5	0.16
9340	0.5	0.028	0.0	250.0	100.00	20.0	0.45
9487	1.0	0.079	0.05	20.0	6.46	9.0	0.16

Table 4. Best fit exponentially decaying star burst SFH (EXP) models to the observations. This table lists the age, mass, extinction, metallicity, and e-folding time τ that resulted in the lowest values of $\chi^2_{\nu c}$. Objects that failed to be properly fitted at the 95% confidence level are indicated with a *.

UID	Age 10^6yr	Mass $10^8 M_\odot$	τ Gyr	Av	Z $\%Z_\odot$	$P(\chi^2_{\nu c} > \chi^2_{\nu c_0})$	$\mathrm{Age_{max}}$ 10^6yr	$\mathrm{Mass_{max}}$ $10^8 M_\odot$
631	9.0	0.17	1.2	0.2	250.0	64.76	200.0	2.2
712	4.5	0.048	0.005	0.0	250.0	94.09	300.0	2.4
4442*	0.5	0.022	1.0	0.0	20.0	1.00	0.5	0.022
5183*	3.0	0.14	0.005	0.6	2.0	3.38	3.0	0.14
5225	5.0	0.22	0.001	0.05	0.5	54.41	300.0	3.9
6139	20.	3.0	0.001	0.4	0.5	80.54	150.0	4.7
9040*	2.5	0.21	0.001	0.0	2.0	0.03	2.5	0.21
9340	1.0	0.061	0.001	0.0	0.5	100.00	100.0	0.46
9487	3.0	0.064	0.0125	0.0	20.0	6.67	15.0	0.13

Table 5. Best double instantaneous burst SFH (2BP) fits to observations. This table lists the age, the total mass, extinction of the object, as well as the age of the second burst and the fraction of the total stellar mass it contains,. that resulted in the lower values of $\chi^2_{\nu c}$. Objects that failed to be properly fitted at the 95% confidence level are indicated with a *.

UID	Age	Mass	2nd Burst		Av	$P(\chi^2_{\nu c} > \chi^2_{\nu c_0})$	$\text{Age}_{\max}$	$\text{Mass}_{\max}$
	10^6yr	$10^8 M_\odot$	Age (10^6yr)	Mass (%)			10^6yr	$10^8 M_\odot$
631	1200.	2.3	3.5	5	0.2	53.26	1200.	5.85
712	16.	0.11	3.0	50	0.2	94.31	1010.	3.67
4442*	2.0	0.023	1.0	1	0.0	0.77	2.0	0.0226
5183*	17.	0.19	13.	1	0.2	3.28	17.	0.186
5225	4.5	0.20	0.5	2	0.0	56.42	1000.	11.5
6139	20.	1.48	4.5	10	0.2	81.28	1006.	8.64
9040*	7.0	0.23	2.5	1	0.0	0.04	7.0	0.23
9340	1.5	0.032	1.0	99	0.0	100.00	1200.	1.26
9487	1.0	0.12	0.5	8	0.15	6.30	1200.	0.363

els appearing to be models with low values for the τ parameter. The double burst scenario (2BP) led to mass estimates that were on average twice that of the other two SFH models. The latter was expected since the 2BP scenario was conceived to allow for a larger stellar mass estimates by asking the question of how large of a fraction of the stellar population of a GRAPES LAE could in fact be in the form of an older stellar population which a lower mass-to-light ratio. The differences in the mass estimate derived using our three distinct SFH models should be kept in mind when comparing the results presented here with those in the literature. Finkelstein et al. (2007), who observed narrow band selected Lyman-α sources as part of the Large Area Lyman Alpha (LALA) survey, derived masses for 22 of their sources and estimated their masses to be in the range of 2×10^7 $M_\odot$ to 2×10^{10} $M_\odot$. They used the best fit of an exponentially decaying burst model (similar to our EXP SFH model). The masses we derived for the GRAPES LAEs, using the best fitting EXP SFH models (Table 4), are about a factor of ten times lower that those found by Finkelstein et al. (2007), with a mass range varying from $0.1 - 3.4 \times 10^8$ $M_\odot$. The largest mass estimates, shown in Table 4 do not exceed 5×10^8 $M_\odot$. Using recent observations of $z \approx 5.7$ Lyman-α sources in the GOODS-N field and a simple SSP model, Lai et al. (2007) estimated the mass of their three sources to be in the range of $1.4 - 5 \times 10^9$ $M_\odot$, overall consistently with the results from Finkelstein et al. (2007) but, again, significantly larger than the largest Lyman-α mass estimates we derived using our SSP SFH models ($0.1 - 5 \times 10^8$ $M_\odot$), or even our 2BP SFH models ($0.1 - 12 \times 10^8$ $M_\odot$). These differences in mass estimate are unlikely to be caused by our respective choices of BC03 templates. Indeed, they are most likely the results of our reach to fainter luminosities (by nearly two AB magnitudes), and hence masses. Our sample was not selected based on the presence of a strong broad band continuum emission and hence might constitute a more complete sample (at least in term of masses) of LAEs. As they stand, the GRAPES LAEs are objects that appear to be significantly less massive than previously observed LAEs at high redshifts, as well as LBGs such as the i dropouts population from Eyles et al. (2005) (with estimated masses of $\approx 1.3 - 3.8 \times 10^{10}$ $M_\odot$). This is consistent with these objects being observed to produce most of their light in the rest-frame UV (i.e. a young stellar population with a relatively lower mass-to-light ratio) and to be either faint (e.g. objects 712, 9487) or even undetected (e.g. objects 4442, 5183, 9040, and 9340) in the rest-frame optical where one would expect light produced by an older, higher mass-to-light ratio stellar population.

We can furthermore examine the star formation rate (SFR) of the HUDF LAEs using either their Lyman-α line luminosities, listed in Table 1, or their rest-frame UV luminosities (Kennicutt 1998). We can additionally use the SFR estimates that the BC03 code produces when generating models. Using the Lyman-α fluxes listed in Table 1, we derive SFRs that

are consistently low for all sources, with an average SFR of 7.8 ± 3.2 $M_\odot$ yr^{-1}. Similarly, the BC03 SFR estimates imply an equally and systematically low SFR of 3.6 ± 2.0 $M_\odot$ yr^{-1}. SFR estimates derived using observed broad band rest-frame 2500Å UV are much more uncertain and result in a higher average SFR of 18.9 ± 22.9 $M_\odot$ yr^{-1}. However, and independently of which of these SFR estimates we consider, the low mass estimates we derived for the HUDF LAEs imply that they have had ample time to form their stars by the observed redshifts, even with an SFR that is only a few $M_\odot$ yr^{-1} . Strictly speaking, there is no need for the SFR of these objects to have been higher in the past, as it was the case for the objects observed by Yan et al. (2006). Higher SFR values would in fact cause these objects to have assembled their stellar masses even more quickly. Based on the observed SFR alone, the HUDF LAEs should have started to form stars no earlier than a few $\times 10^6$ years before we observed them, unless their SFR was significantly lower in the past, consistently with the fact that we have derived low ages for these objects.

We are likely to have found very young and very low mass Lyman-α emitters that formed recently as a result of reporting on a whole sample of Lyman-α sources, including objects that were not detected in the rest-frame optical bands. The IRAC observations, when properly accounting for contamination from neighboring objects, provided stringent limits to the maximum stellar mass that these objects could have. It is noteworthy to note that Gawiser et al. (2006) inferred, using a stack of 18 Lyman-α candidates at $z \approx 3.1$ Lyman-α , that Lyman-α sources at this redshift should have an average mass that is on the order of 5×10^8 $M_\odot$, using models with constant SFH (equivalent to our EXP models with large values of the e-folding time τ). In this paper, we have presented direct observations of 9 such young, low mass LAEs.

We conclude that, independently of SFR, metallicities, and extinction, the GRAPES HUDF LAE population is a population of very young objects with low stellar masses of a few $M_\odot$. There is no easy way to make these objects intrinsically more massive while keeping them intrinsically blue and without violating the IRAC flux estimates and upper limits shown in Table 3. We did derive somewhat larger stellar mass estimates for these objects when we assumed that most of their stars formed at $z >> 10$ in our 2BP models, but the inferred mass of the GRAPES LAEs remained small when compared to previously observed Lyman-α sources.

8. Conclusion

As part of the GRAPES slitless spectroscopic survey of the HUDF, we indentified a sample of faint LAE galaxies at $4.0 < z < 5.7$. These objects were selected solely based on the detection of Lyman-α emission in their low resolution ACS slitless spectra. These

spectra allowed us to identify LAEs down to extremely faint Lyman-α luminosities ($> 2.3 \times 10^{42}$ erg s^{-1}). The further existence of deep, space and ground based observations of these objects, ranging all the way from the rest frame UV to the rest frame optical allowed us to set strong constraints on the masses of these objects. We found that these objects were usually best fitted by models with low extinction and low metallicities. While we attempted to create models using various SHF scenarios, both to compare our results to previous work, and to attempt to maximize our mass estimates for these sources, we systematically derived relatively low masses. We conclude that the HUDF LAEs are sources with masses that are significantly lower, by several order of magnitudes, than previously observed LBGs at these redshifts and that they are also significantly less massive than previously observed LAEs at high redshifts. The GRAPES LAEs, with derived star formation rates of a ≈ 8 M$_\odot$ yr^{-1} and stellar mass estimates that are likely to be no larger than a few times 10^8 M$_{\rm sun}$ must have been formed quickly, unless their SFR was significantly lower earlier on. The mean number density of the GRAPES HUDF LAEs, uncorrected for completeness, is $\approx 1.25 \pm 0.04 \times 10^{-4}$ Mpc^{-3}. The LAEs sources described in this paper are potentially the youngest and least massive galaxies observed to date and at a time when our Universe was just about $\approx$ 1Gyr old.

This work was supported by grants GO-09793.01-A, GO-10530.11-A and AR-10299.01-A from the Space Telescope Science Institute, which is operated by AURA under NASA contract NAS5-26555. We would like to thank Haojing Yan for his help identifying potential X-ray counterparts to the HUDF LAEs using the available Chandra data.

REFERENCES

Baldry, I. K., & Glazebrook, K. 2003, ApJ, 593, 258

Beckwith, S. V. W., et al. 2006, AJ, 132, 1729

Bell, E. F., McIntosh, D. H., Katz, N., & Weinberg, M. D. 2003, ApJS, 149, 289

Bertin, E., & Arnouts, S. 1996, A&AS, 117, 393

Bruzual, G., & Charlot, S. 2003, MNRAS, 344, 1000

Bunker, A. J., Stanway, E. R., Ellis, R. S., & McMahon, R. G. 2004, MNRAS, 355, 374

Calzetti, D., Armus, L., Bohlin, R. C., Kinney, A. L., Koornneef, J., & Storchi-Bergmann, T. 2000, ApJ, 533, 682

Chary, R.-R., Stern, D., & Eisenhardt, P. 2005, ApJ, 635, L5

Conselice, C. J., Bershady, M. A., & Jangren, A. 2000, ApJ, 529, 886

Daddi, E., et al. 2005, ApJ, 626, 680

Dickinson, M., Papovich, C., Ferguson, H. C., & Budavári, T. 2003, ApJ, 587, 25

Dow-Hygelund, C. C., et al. 2005, ApJ, 630, L137

Dawson, S., et al. 2004, ApJ, 617, 707

Dow-Hygelund, C. C., et al. 2006, ArXiv Astrophysics e-prints, arXiv:astro-ph/0612454

Egami, E., et al. 2005, ApJ, 618, L5

Eyles, L. P., Bunker, A. J., Stanway, E. R., Lacy, M., Ellis, R. S., & Doherty, M. 2005, MNRAS, 364, 443

Eyles, L. P., Bunker, A. J., Ellis, R. S., Lacy, M., Stanway, E. R., Stark, D. P., & Chiu, K. 2007, MNRAS, 374, 910

Ferguson, H. C., et al. 2004, ApJ, 600, L107

Finkelstein, L. S., Rhoads, J. E., Malhotra, S., Pirzkal, N., Wang, J. 2007, in preparation

Gawiser, E., et al. 2006, ApJ, 642, L13

Giacconi, R., et al. 2002, ApJS, 139, 369

Giavalisco, M., et al. 2004, ApJ, 600, L93

Tayler, J. R., *An introduction to error analysis* (University Science Books, 1997), Appendix D

Isobe, T., Feigelson, E. D., & Nelson, P. I. 1986, ApJ, 306, 490

Kennicutt, R. C., Jr. 1998, ARA&A, 36, 189

Labbé, I., Bouwens, R., Illingworth, G. D., & Franx, M. 2006, ApJ, 649, L67

Lai, K., Huang, J.-S., Fazio, G., Cowie, L. L., Hu, E. M., & Kakazu, Y. 2007, ApJ, 655, 704

Malhotra, S., & Rhoads, J. E. 2004, ApJ, 617, L5

Madau, P. 1995, ApJ, 441, 18

Meier, D. L. 1976, ApJ, 207, 343

Mobasher, B., et al. 2005, ApJ, 635, 832

Ouchi, M., et al. 2003, ApJ, 582, 60

Peng, C. Y., Ho, L. C., Impey, C. D., & Rix, H. 2002, AJ, 124, 266

Pirzkal, N., et al. 2004, ApJS, 154, 501

Pirzkal, N., et al. 2006, ApJ, 636, 582

Rhoads, J. E., & Malhotra, S. 2001, ApJ, 563, L

Rhoads, J. E., et al. 2003, AJ, 125, 1006

Rhoads, J. E., et al. 2005, ApJ, 621, 582

Salpeter, E. E. 1955, ApJ, 121, 161

Schaerer, D., & Pelló, R. 2005, MNRAS, 362, 1054

Somerville, R. S., Lee, K., Ferguson, H. C., Gardner, J. P., Moustakas, L. A., & Giavalisco, M. 2004, ApJ, 600, L171

Stark, D. P., Bunker, A. J., Ellis, R. S., Eyles, L. P., & Lacy, M. 2006, ArXiv Astrophysics e-prints, arXiv:astro-ph/0604250

Steidel, C. C., Giavalisco, M., Pettini, M., Dickinson, M., & Adelberger, K. L. 1996, ApJ, 462, L17

Stern, D., Bunker, A., Spinrad, H., & Dey, A. 2000, ApJ, 537, 73

Taniguchi, Y., et al. 2005, PASJ, 57, 165

Thompson, R. I., et al. 2005, AJ, 130, 1

Venemans, B. P., et al. 2005, A&A, 431, 793

Xu, C. et al. 2007, in preparation

Yan, H., Dickinson, M., Giavalisco, M., Stern, D., Eisenhardt, P. R. M., & Ferguson, H. C. 2006, ApJ, 651, 24

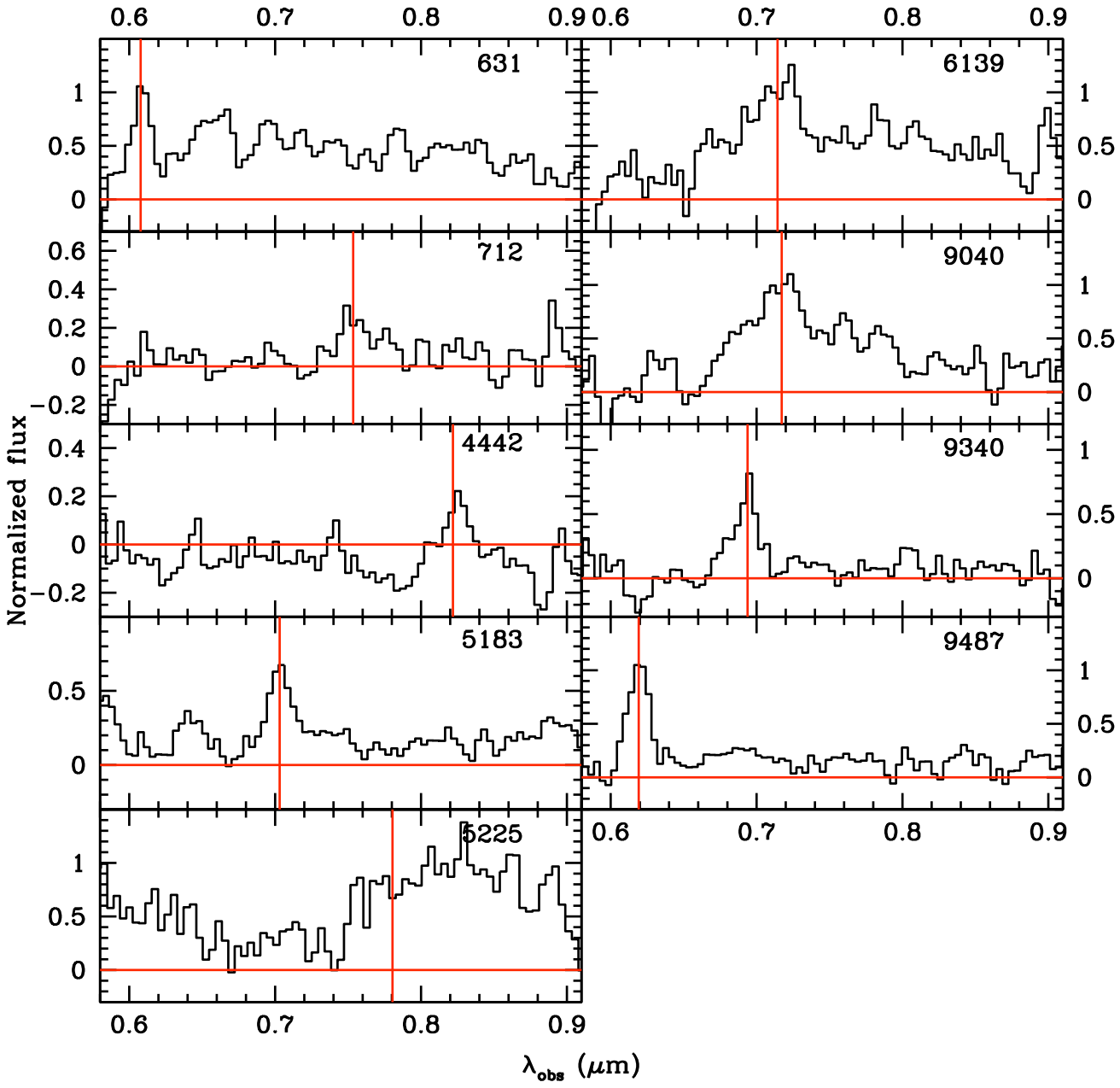

Fig. 1.— ACS G800L grism spectra of the nine Lyman-α galaxies in our sample.

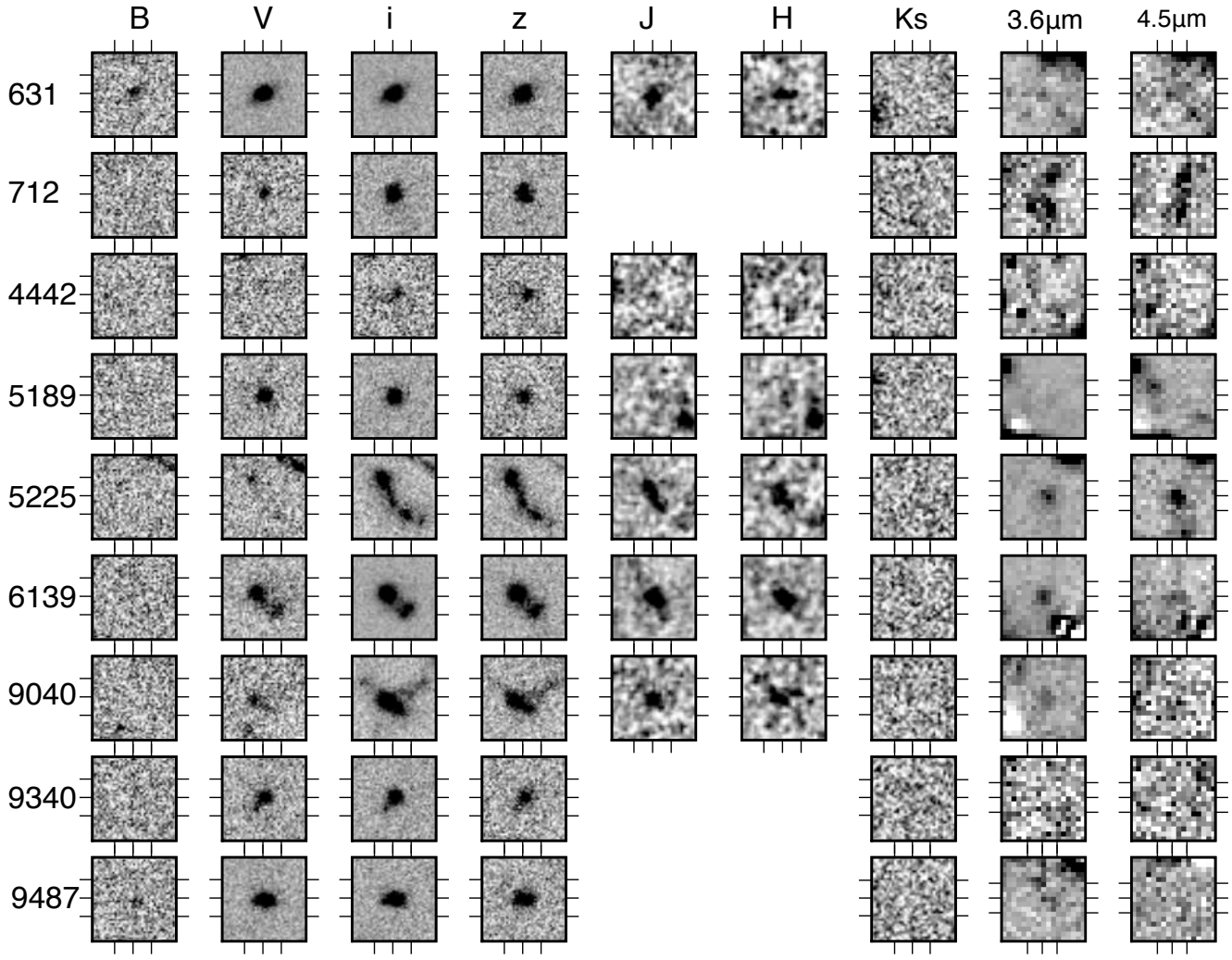

Fig. 2.— ACS, NICMOS, ISAAC and IRAC observations of GRAPES LAEs. The source is at the center of each stamp image. ACS B_{435}, V_{606}, i_{775} and z_{850} band stamps are 1.2"x1.2", NICMOS J_{1100} and H_{1600} band stamps are 2.4"x2.4", ISAAC Ks_{2200}, $IRAC_{3600}$ and $IRAC_{4000}$ band stamps are 5"x5"

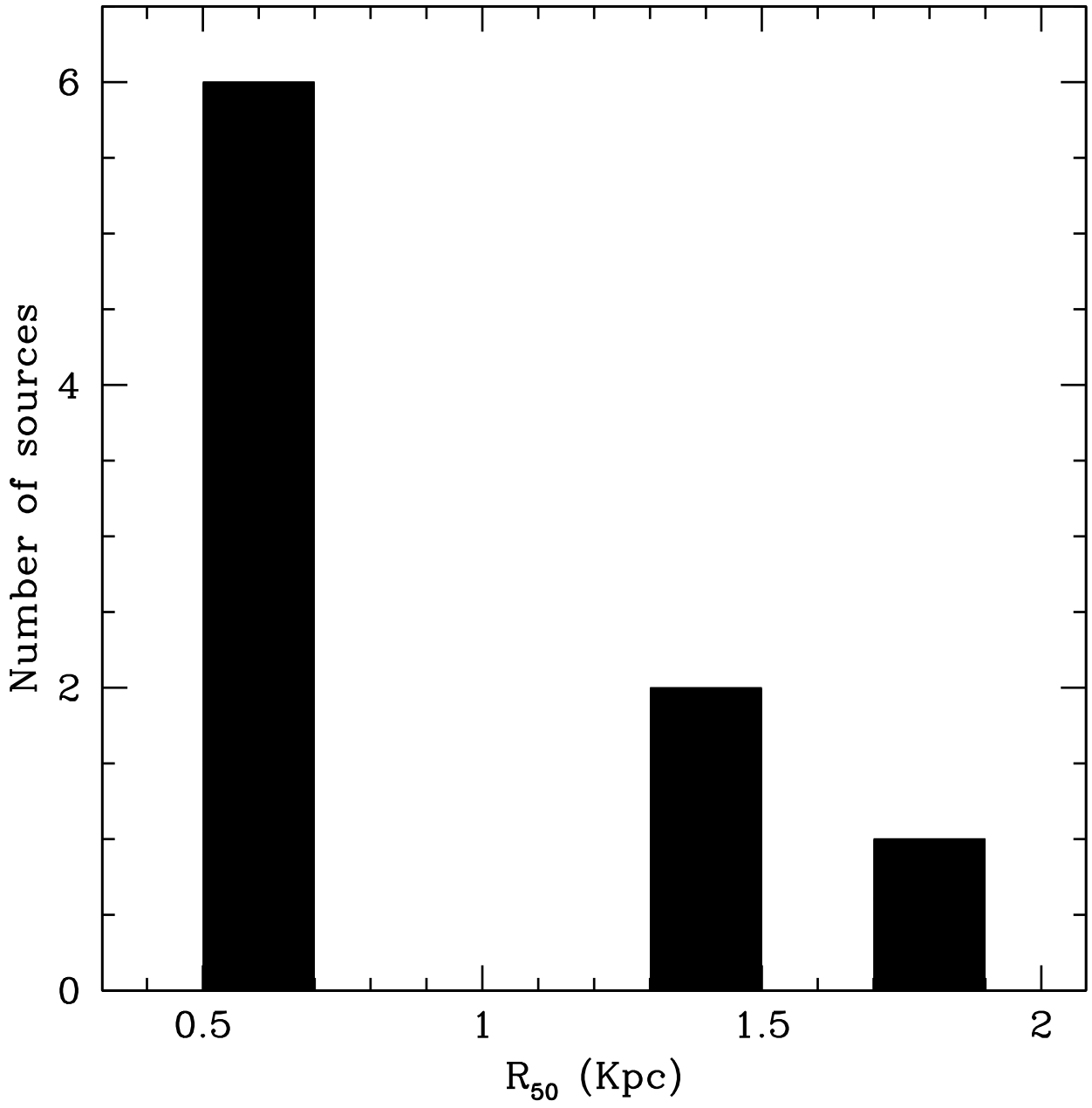

Fig. 3.— Histogram of the measured half-light radius (R_{50}) of the GRAPES LAEs. Most objects are observed to have small R_{50}, with $R_{50} < 1.0$kpc

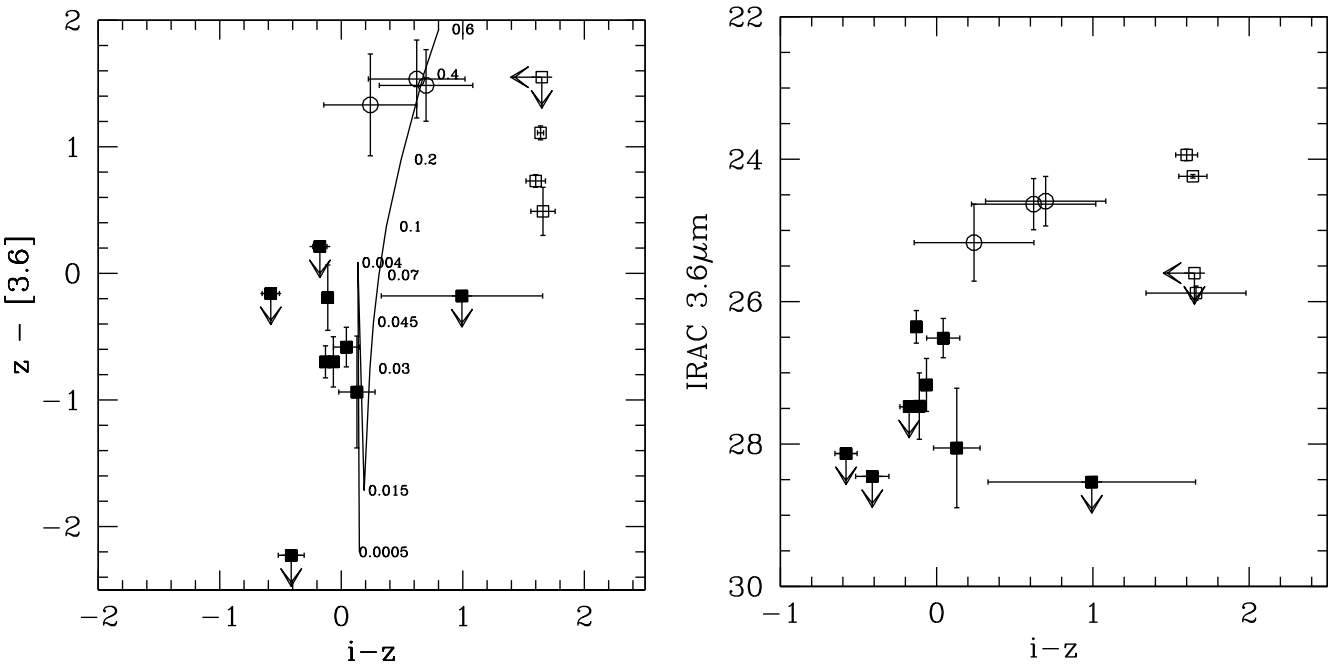

Fig. 4.— Colors of the GRAPES LAEs (solid squares) in the z-3.6μm vs i-z space. These objects appear to be extremely blue, similarly to previously identified high redshift LAEs (circles) from Lai et al. (2007), and significantly bluer than the i drop/LBGs (squares) from Eyles et al. (2005) (Left panel). Colors of a z=5 single burst galaxy is shown as a solid line for comparison with ages shown in Gyr. This points to the GRAPES LAEs to potentially be very young, low extinction objects. Similarly, assuming low values of extinction, these sources appear to be fainter in the rest-frame optical (3.6μm) than either the LBGs or LAEs that were previously observed at these high redshifts (Right panel).

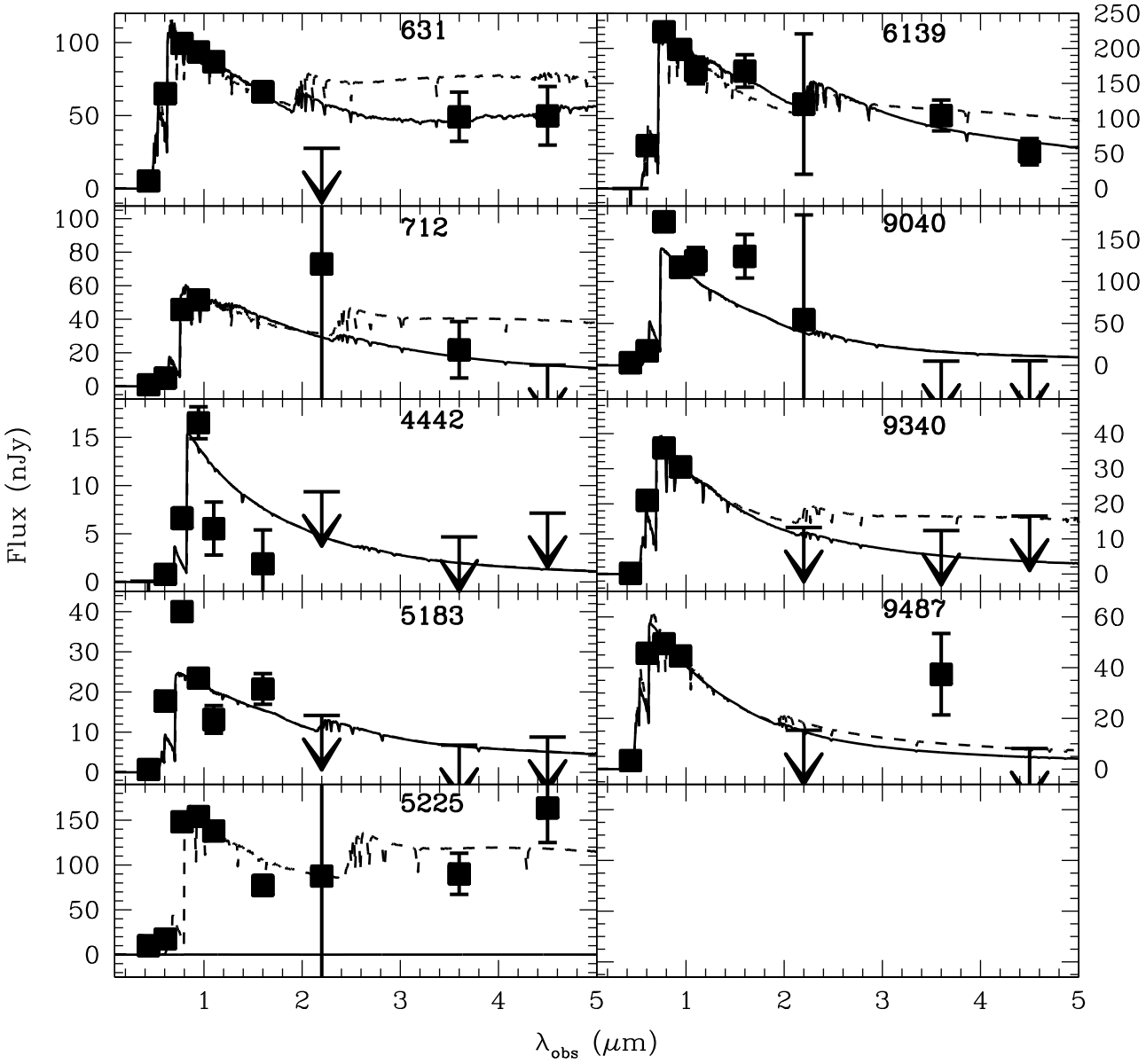

Fig. 5.— Plots of the best (solid line) fitting double instantaneous burst model (2BP) fits to the observations (solid squares) and our 1σ upper limit estimates (arrows). The best, most massive acceptable 2BP models are also shown (dash line). The masses, ages, extinctions of each of these models are listed in Table 5.